

Article

Grain Boundary Characterization and Potential Percolation of the Solid Electrolyte LLZO

Shuo Fu ^{1,2}, Yulia Arinicheva ^{2,3}, Claas Hüter ¹, Martin Finsterbusch ² and Robert Spatschek ^{1,4,*}

¹ IEK-2, Forschungszentrum Jülich, 52425 Jülich, Germany

² IEK-1, Forschungszentrum Jülich, 52425 Jülich, Germany

³ Department of Safety, Chemistry and Biomedical Laboratory Sciences, Faculty of Engineering and Science, Western Norway University of Applied Sciences (HVL), 5020 Bergen, Norway

⁴ JARA-ENERGY, 52425 Jülich, Germany

* Correspondence: r.spatschek@fz-juelich.de

Abstract: The influence of different processing routes and grain size distributions on the character of the grain boundaries in $\text{Li}_7\text{La}_3\text{Zr}_2\text{O}_{12}$ (LLZO) and the potential influence on failure through formation of percolating lithium metal networks in the solid electrolyte are investigated. Therefore, high quality hot-pressed $\text{Li}_7\text{La}_3\text{Zr}_2\text{O}_{12}$ pellets are synthesised with two different grain size distributions. Based on the electron backscatter diffraction measurements, the grain boundary network including the grain boundary distribution and its connectivity via triple junctions are analysed concerning potential Li plating along certain susceptible grain boundary clusters in the hot-pressed LLZO pellets. Additionally, the study investigates the possibility to interpret short-circuiting caused by Li metal plating or penetration in all-solid-state batteries through percolation mechanisms in the solid electrolyte microstructure, in analogy to grain boundary failure processes in metallic systems.

Keywords: all-solid-state batteries; Li plating; grain boundary network; triple junctions



Citation: Fu, S.; Arinicheva, Y.; Hüter, C.; Finsterbusch, M.; Spatschek, R. Grain Boundary Characterization and Potential Percolation of the Solid Electrolyte LLZO. *Batteries* **2023**, *9*, 222. <https://doi.org/10.3390/batteries9040222>

Academic Editors: Chunwen Sun, Siqi Shi and Yongjie Zhao

Received: 3 March 2023

Revised: 31 March 2023

Accepted: 6 April 2023

Published: 8 April 2023



Copyright: © 2023 by the authors. Licensee MDPI, Basel, Switzerland. This article is an open access article distributed under the terms and conditions of the Creative Commons Attribution (CC BY) license (<https://creativecommons.org/licenses/by/4.0/>).

1. Introduction

All-solid-state batteries (ASSBs) belong to the most promising next generation electrochemical energy storage systems [1–3]. A solid electrolyte, one of the key components enabling rechargeable ASSBs, allows safety concerns of the conventional lithium ion batteries to be overcome, substituting flammable organic electrolytes, and offers the potential for a significant improvement of energy density and battery life when metallic lithium is used as an anode [3,4]. Li-ion conducting garnets, in particular $\text{Li}_7\text{La}_3\text{Zr}_2\text{O}_{12}$ (LLZO), satisfy a number of the technological requirements for the application as solid electrolytes in ASSBs, such as high ionic and negligible electronic conductivities, a wide voltage window, as well as chemical and electrochemical compatibility with metallic lithium [5].

However, short-circuiting caused by Li dendrite formation within LLZO solid electrolytes during battery cycling has still been a challenge according to recent publications. Recently, it was shown that LLZO garnets can fail during operation by the development of microcracks due to mechanical stressing, followed by Li intrusion [6]. This effect, however, does not exclude other failure mechanisms, which may be related to the intrinsic microstructure of polycrystalline battery components, commonly found in industrial applications. Ren et al. [7] directly observed that lithium dendrites grow along grain boundaries and through interconnected pores. Aside from these effects, internal lithium plating was observed in isolated pores, which are considered as a trap of electrons and can reduce Li^+ to metallic Li [8,9]. Cheng et al. [10] proved that Li preferentially propagates intergranularly along the grain boundaries in LLZO. Motoyama et al. [4] demonstrated using in situ SEM that Li plating tends to occur at grain boundaries and triple junctions. In order to enable large-scale applications such as electric vehicles, dendrite formation and propagation should be prevented during cycling over a wide range of current densities [11] and

operating temperatures [12]. Key factors for dendrite formation or propagation in LLZO are relative density or porosity [7], interface properties (contact between the electrolyte and Li, roughness of the electrolyte surface, defects) [4,13], microstructure (i.e., grain size and boundary character) [11,14,15], etc. These aspects cover a large fraction of accessible characteristics of grain boundaries in the context of Li dendrite penetration, but they do not yet consider the influence of the connectivity of the grain boundary network. Such conclusions would require a detailed analysis of the grain boundary structures, which has not been performed so far. Due to the complexity of this topic, we pursue in this using an experimental analysis of the grain boundary and trijunction characteristics, and on top of this a critical inspection of percolation models, to shed light on the question, whether such an approach, which is well established in other materials science disciplines, may also be useful for all-solid-state battery materials.

In general, percolation is the formation of a conducting path through a network. The random occupation of sites or bonds in connected lattices or networks is referred to as site percolation and bond percolation, respectively. Percolation works in an all-or-nothing mode and it is a threshold phenomenon, which means that if the threshold value is achieved, the percolation is certain to happen. The description of grain-boundary-related failure in terms of percolation theory has been established with investigations on austenitic steels [16]. The prediction of the percolation threshold of an intergranular failure for 3D grain boundary networks at 23% of active bonds is supported by experimental findings in Ref. [17]. With the derivation of the influence of crystallographic constraints (e.g., the Σ -product rule) on percolation in 2D and 3D grain boundary networks, the substantial discrepancy of the percolation threshold between constrained and non-constrained networks could be explained. Aside from the mentioned applications of percolation theory to grain boundary failure driven by corrosion, Perrior et al. [18] found that the vacancy-mediated cation diffusion in disordered pyrochlore is enhanced once a percolation network is established. A similar effect is also observed by Lee et al. [19] for Li diffusion in lithium transition metal oxides, where the diffusion is facile along the percolating network of channels with excess content of Li. However, these observations only provide indications of preferred cation diffusion in percolating networks, whereas the interpretation of the Li plating along grain boundaries and triple junctions in solid electrolytes in the spirit of a percolation analysis remains questionable. Depending on the answer to this question, it may be conceivable that grain boundary degradation phenomena such as Li plating or dendrite propagation in a polycrystalline solid electrolyte could be evaluated using percolation theory as a step towards grain boundary engineering to control the fraction and distribution of specific grain boundaries, which are resistant to intergranular percolation phenomena, in analogy to the intergranular corrosion in austenitic stainless steels [20,21]. To test such a hypothesis, it is necessary to first overcome the lack of careful investigations into the grain and grain boundary structure of LLZO, which is essential for the understanding of the mechanical and electrochemical performance of the solid electrolyte. As the direct test of such a potential picture is difficult from an experimental perspective alone, indirect and theoretically supported arguments are needed to uphold or counter this hypothesis.

Consequently, the present work focuses on the joint experimental and theoretical investigation of the influence of microstructure, and in particular of the grain boundary connectivity, on Li dendrite formation and propagation using percolation theory. The first and main goal of the paper is a detailed analysis of the microstructure and the grain boundaries of LLZO using two different synthesis routes. The second aspect is dedicated to the question of whether established percolation models for intergranular corrosion in metallic systems, for which a deep understanding of the different types of grain boundaries and their resistance to corrosion has been achieved as explained above, can similarly be applied to failure mechanisms in LLZO-based all-solid-state batteries.

2. Materials and Methods

2.1. Experimental Investigations

2.1.1. Synthesis and Fabrication of LLZO Samples

The different grain sizes of LLZO pellets are obtained from two different synthesis routes of the precursor powders, a conventional solid-state reaction (SSR) [22] and a solution-assisted solid-state reaction (SASSR). Then, both precursor powders are sintered using hot-pressing in order to achieve a high density, i.e., close to theoretical density of a defect free and perfect crystal. The optimal sintering temperature for each precursor powder was determined from the onset temperature for shrinkage from densification curves obtained by dilatometric analysis.

For the solid-state reaction, the starting reagents listed here are mixed in stoichiometric amounts: LiOH·H₂O (98%, Merck, Darmstadt, Germany, with 20 mol% excess for the compensation of lithium loss during the next calcination and sintering steps), La₂O₃ (99.9%, Merck, Darmstadt, Germany, dried at 900 °C for 10 h), ZrO₂ (99.5%, Treibacher, Treibach, Austria), Ta₂O₅ (99.5%, Inframat Corp., Manchester, USA) and 5 mol% α -Al₂O₃ (99.9%, Inframat Corp., Manchester, NH, USA, as a sintering additive). The reaction mixture is homogenized in a motor grinder (Retsch RM 200) for 30 min at a rotational speed of 100 rpm. Next, the resulting powder is pressed into pellets and tempered in an Al₂O₃ crucible at 850 °C for 20 h with a heating and cooling rate of 5 K/min in air. The pellets are subsequently ground and pressed into pellets and calcined at 1000 °C for 20 h.

Alternatively, for the solution-assisted solid-state reaction, the starting reagents LiNO₃ (99%, water-free, Alfa Aesar, Ward Hill, MA, USA, with 20 mol% excess), ZrO(NO₃)₂·6H₂O (99%, Sigma-Aldrich, St. Louis, MO, USA) and La(NO₃)₃·6H₂O (99%, Alfa Aesar, Ward Hill, USA) are dissolved in distilled water. Then, C₁₀H₂₅O₅Ta (99.9%, Strem Chemicals, Newburyport, MA, USA) is slowly added dropwise to the metal salt solution upon continuous stirring on a magnetic stirrer. The reaction mixture is dried at 80 °C overnight and calcined at 400 °C for 3 h to burn out the organic residues, and then at 750 °C for 4 h in an Al₂O₃ crucible.

After both synthesis routes of the precursor powders, the high density of the pellets is achieved by a hot-pressing (HP) technique. The calcined pellets are thoroughly ground in an agate mortar and the resulting powders are pre-pressed at 100 MPa into pellets with a diameter of 13 mm using a uniaxial press (Paul-Otto Weber). For the powder from the solid-state synthesis, the hot-pressing of the pellets is conducted at 1150 °C and 50 MPa under a flowing N₂ atmosphere for 3 h. Similarly, for the powder from the solution-assisted solid-state synthesis, the hot-pressing is conducted at 1075 °C and 50 MPa under the same flowing N₂ atmosphere for 3 h. The hot-pressed pellets are then cut into ~0.65 mm thick slices by using a diamond saw under ethanol.

2.1.2. Sample Characterization

The purity of the phases and the crystal structure of the hot-pressed LLZO samples are characterized by X-ray diffraction (XRD) using the Bruker D4 Endeavor diffractometer with Cu-K_α radiation in a 2θ range from 10° to 80° with a step size of 0.02° at room temperature.

The relative densities of the HP pellets are determined via Archimedes's method using water as a liquid medium.

Inductively coupled plasma optical emission spectroscopy (ICP-OES) (Thermo Elemental, IRIS Intrepid) is used to determine the elemental composition of the hot-pressed LLZO samples. For this, 50 mg LLZO samples are dissolved in a solution of 2 g ammonium sulphate and 4 mL H₂SO₄, until the powder is completely dissolved. The obtained solution is diluted to 50 mL by using distilled water for the ICP-OES analysis. The experimental inaccuracy of ICP-OES analyses is about 3% of the measured concentration.

For the microstructural investigations, the pellets are mechanically ground using SiC sandpapers up to 4000 grit and mirror-polished by a water-free diamond suspension up to 0.5 μm under a 10 N force. In order to remove the surface contamination of the LiOH and Li₂CO₃ layer and to reduce the surface roughness, thermal etching under flowing

Ar for 2 h at 800 °C and the plasma-etching in the glove box (with Ar atmosphere) are conducted before polishing. For the scanning electron microscopy (SEM) and electron backscatter diffraction (EBSD) measurements, the pellets are transferred into the chamber immediately after the final polishing step is finished, in order to minimize the surface contamination, e.g., by carbonate formation, from the exposure to the moist air. The SEM of the precursor powders and HP pellets and the EBSD of the HP pellets are performed on the scanning electron microscope JEOL JSM-7000F (2006) with a combined EDX/EBSD-System EDAX Pegasus.

The EBSD measurements are conducted at an accelerating voltage of 30 kV with a lateral resolution of 1.2 nm and the HP pellets are tilted at 70° toward the EBSD detector. A working distance of 20 mm and a step size of 1 μm are used for EBSD mapping. The scanning area of the HP pellets is large enough (500 μm × 1000 μm), so that a sufficient statistical accuracy can be achieved with a huge number of investigated grains and grain boundaries. The grain boundary (GB) and triple junction (TJ) analysis of LLZO pellets is conducted from the collected EBSD data using the open source toolbox MTEX [23] in Matlab. The grain boundary misorientation angle θ is calculated from the rotation angle with respect to the crystal symmetry, which can be obtained from the Euler angles (ϕ_1, Φ, ϕ_2) of the adjacent grains.

2.2. Percolation Models

As reported in Ref. [20], percolation theory can predict intergranular corrosion degradation preferentially occurring along the grain boundaries in steels. The basic idea includes a binary classification of the grain boundaries present in the material, i.e., coincidence site lattices (CSLs) and random grain boundaries. The CSLs are grain boundaries for which the adjacent periodic crystal lattices have common atomic positions in order to obtain the most stable energetic state [24,25]. They are characterised by the quantity Σ , which is the density of the coincident sites in crystal lattice [26,27]. For example, $\Sigma 5$ means that every fifth lattice site is a coincidence site. This distinction reflects whether an individual grain boundary is expected to block percolation of ions (“resistant grain boundary” for CSLs) or support it (“susceptible grain boundaries” for random grain boundaries). In the analysis of grain boundary microstructures in polycrystalline materials, grain boundaries with a misorientation angle $\theta \leq 15^\circ$ are considered as low angle grain boundaries (LAGBs) based on the dislocation structure [26]. LAGBs consist of isolated dislocations and are not participating in the percolating process [20,21]. High angle grain boundaries ($\theta > 15^\circ$) with low- Σ values are defined as CSL boundaries (CSLs) and Brandon’s criterion [25], $\Delta\theta = 15^\circ / \Sigma^{0.5}$, is used to calculate the deviations from CSLs in the cubic structure. Other grain boundaries with high- Σ value or grain boundaries that cannot be described by CSLs, i.e., the misorientation angle of the grain boundary is far beyond the deviations from Brandon’s criterion, are considered as random grain boundaries. This classification proposes a distinction between grain boundaries, which may be susceptible to Li plating, and resistant grain boundaries. According to the raised hypothesis, fatal failure could occur in such a network if a percolating path of susceptible grain boundaries may form inside the solid electrolyte, connecting anode and cathode.

In addition to the first picture, where grain boundaries themselves are considered as the limiting elements to form a conducting network, the focus of the second picture is on the triple junctions, where three adjacent grain boundaries come together. The connection between two conducting grain boundaries has to cross the triple junction, and the triple junction itself can be considered as a conducting or blocking element. Hence, according to this picture, triple junctions may play an important role in the connectivity of a grain boundary network. The triple junctions in the microstructure can be distinguished by the number of CSLs connected, namely the “resistant triple junctions” with 3-CSL or 2-CSL connected, and the “susceptible triple junctions” with 1-CSL or 0-CSL connected [28,29], which are schematically shown in Figure 1.

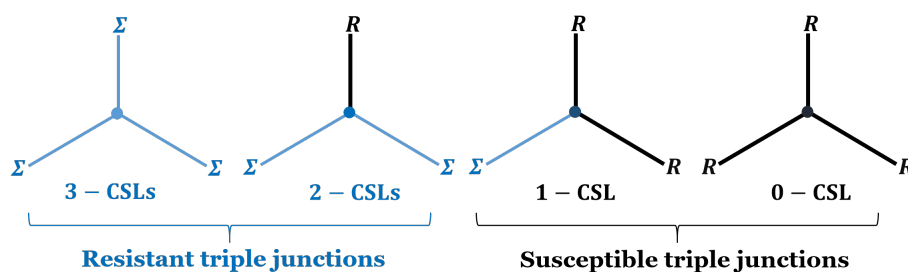


Figure 1. Schematic sketch of two different types of triple junctions in terms of percolation probability: the triple junctions with 3-CSL and 2-CSL are resistant triple junctions, which are expected to block Li percolation; the triple junctions with 1-CSL and 0-CSL are susceptible triple junctions, which are potentially active for the Li plating process. Here, thin blue lines denote CSLs, while bold black lines denote random grain boundaries.

Only the triple junctions with at least two random grain boundaries are considered to be susceptible to percolation, which are potentially the active entities in the process of Li plating and percolation along grain boundaries in the solid electrolyte.

In a two-dimensional calculation of the homogeneous bond percolation for the hexagonal or honeycomb lattice, which is assumed to approximately represent polycrystalline microstructures considering the topological rather than the geometric nature appropriately, the theoretical percolation threshold (p_c) of the susceptible grain boundaries/triple junctions is about 65% (fraction of resistant grain boundaries/triple junctions is 35%) [30,31]. This percolation threshold is confirmed by both analytical models [32] and experimental observations [33], since the honeycomb lattice can reflect the connectivity of the polycrystalline structure. Based on the aforementioned distinction of grain boundaries and triple junctions, we can investigate whether such a percolation model is suitable for the lithium plating failure across grain boundary networks in the sense of homogeneous bond percolation.

3. Results and Discussion

3.1. Microstructural Analysis

Dense LLZO samples (99% of the theoretical density of a perfect crystal) with larger grains (LG) and smaller grains (SG) are obtained by hot-pressing of LLZO precursor powders with different particle morphologies (see Figure 2 and Table 1), synthesized by the conventional solid-state method and solution-assisted solid-state synthesis method, respectively.

Table 1. Summary of synthesis route information leading to different grain sizes in the samples.

| Sample | Powder Synthesis | Surface Roughness | Grain Size |
|--------|------------------|-------------------------|------------------------------|
| SG | SASSR | $147 \pm 10 \text{ nm}$ | $7.25 \pm 4.29 \mu\text{m}$ |
| LG | SSR | $202 \pm 10 \text{ nm}$ | $10.30 \pm 6.07 \mu\text{m}$ |

The actual composition for the hot-pressed LLZO obtained from both synthesis routes is $\text{Li}_{6.3}\text{Al}_{0.01}\text{La}_3\text{Zr}_{1.6}\text{Ta}_{0.4}\text{O}_{12}$, according to the ICP-OES analysis. XRD analysis confirms the formation of the pure cubic garnet phase (space group $\text{Ia}\bar{3}\text{d}$) of the SG and LG samples. The SEM micrographs of the surfaces of the hot-pressed LLZO samples and corresponding XRD patterns are presented in Figure 3.

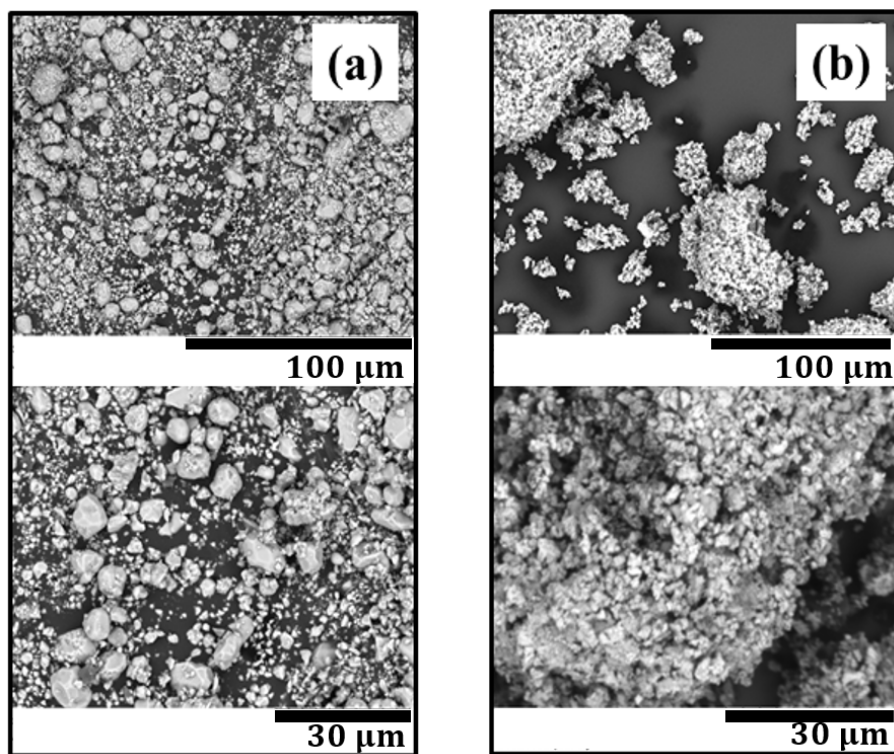


Figure 2. SEM images of precursor powders synthesized from: (a) conventional solid-state reaction (SSR) and (b) solution-assisted solid-state reaction (SASSR).

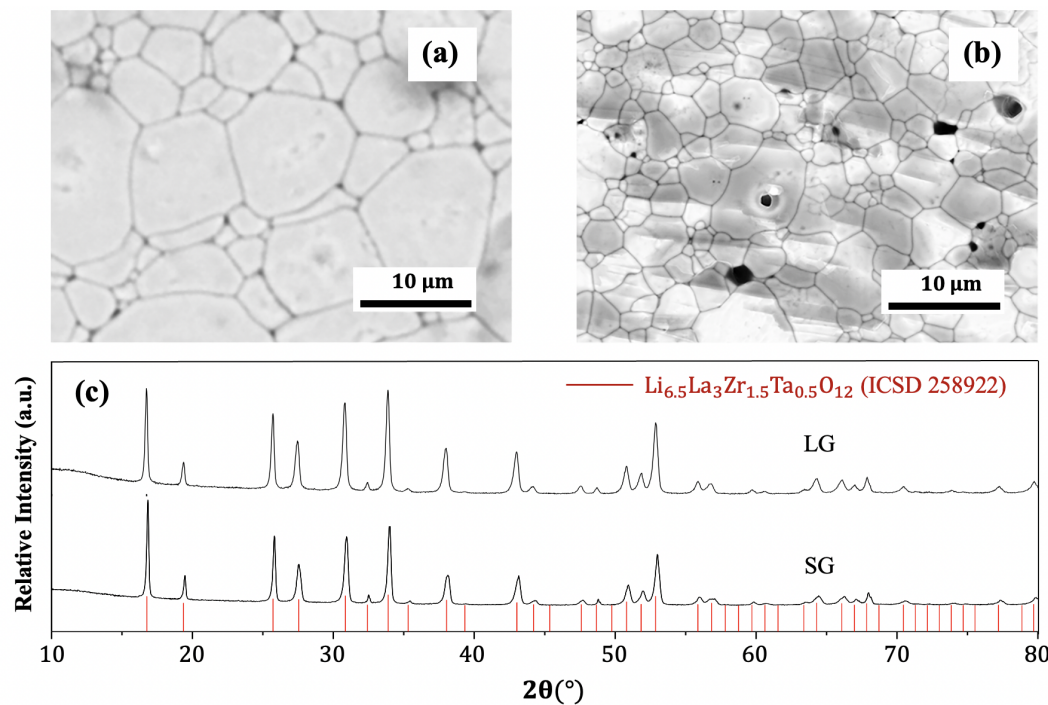


Figure 3. SEM images of the pellets with (a) larger grains (LG) and (b) smaller grains (SG). The visible surface pores are removed by polishing before further processing. The corresponding (c) XRD patterns of the pellets are compared with the cubic phase of $\text{Li}_{6.5}\text{La}_3\text{Zr}_{1.5}\text{Ta}_{0.5}\text{O}_{12}$, calculated from the results of Awaka et al. [34].

3.2. Grain Boundary and Triple Junction Classification

From the EBSD grain orientation maps of the hot-pressed pellets (Figure 4), the grain size (largest grain diameter) statistics is evaluated and shown in Figure 5.

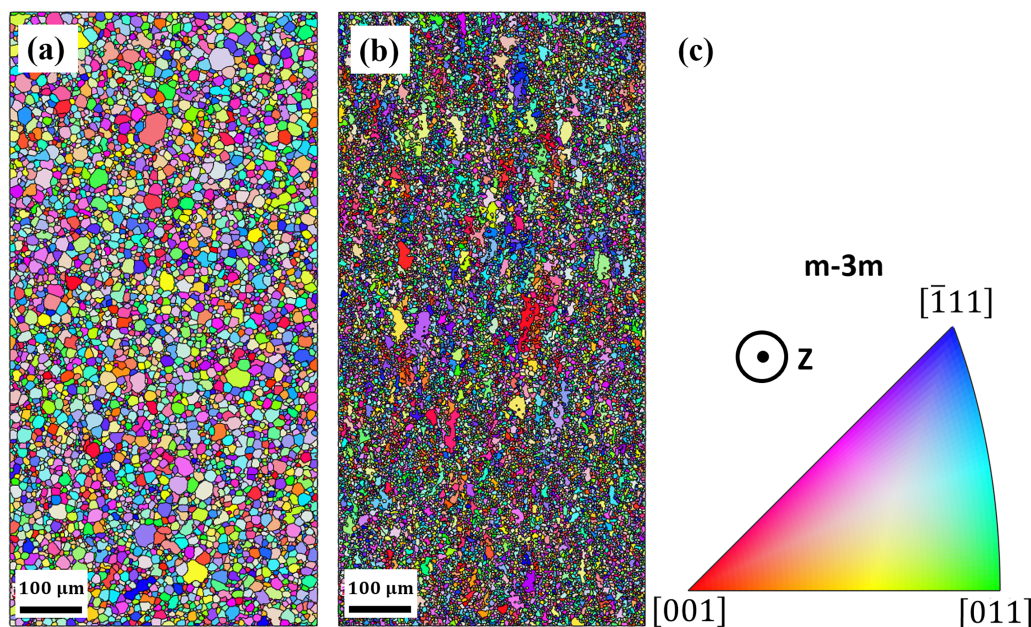


Figure 4. EBSD mean grain orientation maps with grain boundaries in solid black line of the hot-pressed pellets (a) LG, (b) SG and (c) the inverse pole figure [001] to indicate the crystallographic orientations.

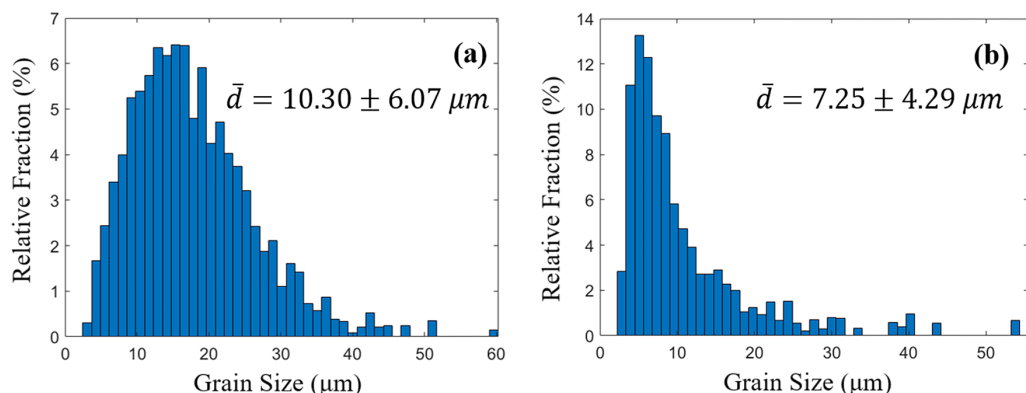


Figure 5. Grain size distribution histograms obtained from EBSD analysis of the hot-pressed pellets (a) LG, (b) SG.

The mean grain size of each hot-pressed pellet and its corresponding standard deviation are summarised in Table 1. For the sample of small grains (SG), the grain size is more centrally distributed than that of the sample of large grains (LG).

The grain boundary misorientation is also investigated from EBSD data and compared with the Mackenzie distribution [35] to determine its randomness (Figure 6).

A wide range of misorientation angles from 15° to 65° is observed in both LG and SG pellets. Apparently, no low angle grain boundaries (LAGBs), which have a misorientation angle below 15° , are detected, and therefore the calculated length fraction of LAGBs is confirmed to be 0%. Hence, all grain boundaries in the pellets are either coincidence site lattices (CSLs) or random grain boundaries. The fraction of grain boundaries with relatively lower misorientation angle (from 15° to 35°) in SG samples is larger than the theoretical Mackenzie distribution, indicating that the grain boundaries in SG pellets prefer to have a lower lattice mismatch. In contrast, in LG samples, the distribution of grain boundary misorientation is in coincidence with the Mackenzie distribution, indicating a non-preferential orientation of the grains.

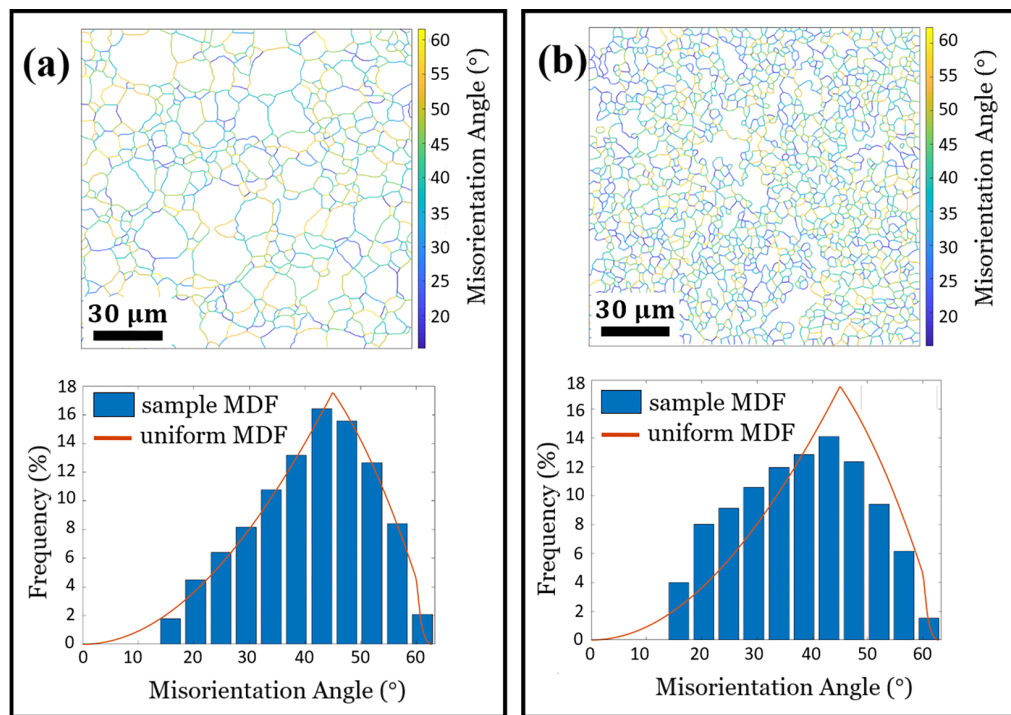


Figure 6. Grain boundary misorientation angle maps and distribution histograms compared with the misorientation density function (MDF) according to the Mackenzie distribution [35] in the selected area of the pellets: (a) LG, (b) SG.

Based on the crystal symmetry and the orientation from the EBSD measurements, we calculate the misorientation angles (θ°) for CSLs (up to $\Sigma 49$) from their Euler angles and evaluate a specific deviation angle ($\Delta\theta^\circ$) for each CSL according to Brandon's criterion [25], $\Delta\theta = 15^\circ/\Sigma^{0.5}$, which is summarised in Table 2.

The grain boundary fraction of each type is given by the length fraction, i.e., the total grain boundary length of one type normalised to the total length of all the grain boundaries. The fraction of different types of triple junctions is given by its number fraction. The evaluation for the grain boundary distribution is conducted through the entire EBSD scanning area of $500 \mu\text{m} \times 1000 \mu\text{m}$. The calculated fraction of CSLs and random grain boundaries are summarised in Table 3.

Table 2. List of CSLs ($\Sigma \leq 49$) with Brandon's criterion in cubic LLZO (CSL type Σ , Euler angles (ϕ_1, Φ, ϕ_2) in degree, misorientation angle θ° and its deviation $\Delta\theta^\circ$).

| Σ | ϕ_1 | Φ | ϕ_2 | θ° | $\Delta\theta^\circ$ |
|----------|----------|--------|----------|----------------|----------------------|
| 3 | 63.43 | 48.19 | 333.44 | 60 | 8.66 |
| 5 | 53.13 | 0 | 0 | 36.87 | 6.71 |
| 7 | 56.31 | 31 | 326.31 | 38.21 | 5.67 |
| 9 | 104.04 | 27.27 | 284.04 | 38.94 | 5 |
| 11 | 108.44 | 35.10 | 288.44 | 50.48 | 4.52 |
| 13a | 22.62 | 0 | 0 | 22.62 | 4.16 |
| 13b | 53.13 | 22.62 | 323.13 | 27.80 | 4.16 |
| 15 | 111.80 | 21.04 | 291.80 | 48.19 | 3.87 |
| 17a | 28.07 | 0 | 0 | 28.07 | 3.64 |
| 17b | 85.24 | 45.10 | 318.37 | 61.93 | 3.64 |
| 19a | 99.46 | 18.67 | 279.46 | 26.53 | 3.44 |
| 19b | 59.04 | 37.86 | 329.04 | 46.83 | 3.44 |
| 21a | 51.34 | 17.75 | 321.34 | 21.79 | 3.27 |

Table 2. Cont.

| Σ | ϕ_1 | Φ | ϕ_2 | θ° | $\Delta\theta^\circ$ |
|----------|----------|--------|----------|----------------|----------------------|
| 21b | 116.57 | 25.21 | 296.57 | 44.42 | 3.27 |
| 23 | 116.57 | 16.96 | 296.57 | 40.46 | 3.13 |
| 25a | 16.26 | 0 | 0 | 16.26 | 3 |
| 25b | 90 | 36.87 | 306.87 | 51.68 | 3 |
| 27a | 105.95 | 15.64 | 285.95 | 35.43 | 2.89 |
| 27b | 101.31 | 22.19 | 281.31 | 31.59 | 2.89 |
| 29 | 79.38 | 34.15 | 312.51 | 46.40 | 2.79 |
| 31 | 113.20 | 29.43 | 293.20 | 52.20 | 2.69 |
| 33a | 97.13 | 14.14 | 277.13 | 20.05 | 2.61 |
| 33b | 119.75 | 14.14 | 299.75 | 33.56 | 2.61 |
| 33c | 68.20 | 40.75 | 338.20 | 58.99 | 2.61 |
| 35 | 50.04 | 19.46 | 329.04 | 34.05 | 2.54 |
| 37a | 18.98 | 0 | 0 | 18.98 | 2.46 |
| 37b | 110.56 | 13.35 | 290.56 | 43.14 | 2.47 |
| 39a | 54.46 | 26.18 | 324.46 | 32.20 | 2.40 |
| 39b | 83.99 | 29.33 | 317.12 | 50.13 | 2.40 |
| 39c | 85.60 | 41.96 | 302.47 | 50.13 | 2.40 |
| 41a | 12.68 | 0 | 0 | 12.68 | 2.34 |
| 41b | 108.44 | 17.97 | 288.44 | 40.88 | 2.34 |
| 43a | 102.53 | 12.38 | 282.53 | 27.91 | 2.29 |
| 43b | 76.87 | 45.76 | 324.25 | 60.77 | 2.29 |
| 45a | 75.96 | 27.27 | 309.09 | 36.87 | 2.24 |
| 45b | 81.87 | 38.94 | 315 | 53.13 | 2.24 |
| 47 | 108.44 | 23.81 | 288.44 | 43.66 | 2.19 |
| 49a | 113.96 | 11.60 | 293.96 | 43.57 | 2.14 |
| 49b | 116.57 | 33.20 | 296.57 | 49.23 | 2.14 |

Table 3. Summary of grain boundary characteristics for small grain (SG) and large grain (LG) samples of HP-LLZO.

| Property | SG | LG |
|-------------------------------------|-------|-------|
| \bar{d} (μm) | 7.25 | 10.30 |
| Grain Boundary Distribution | | |
| CSL% | 12.29 | 13.31 |
| $\Sigma 3\%$ | 1.42 | 1.78 |
| $\Sigma 9\%$ | 1.00 | 0.91 |
| $\Sigma 27\%$ | 0.71 | 0.65 |
| Triple Junction Distribution | | |
| $f_{0CSL}\%$ | 62.65 | 61.55 |
| $f_{1CSL}\%$ | 32.05 | 31.70 |
| $f_{2CSL}\%$ | 5.02 | 6.20 |
| $f_{3CSL}\%$ | 0.27 | 0.54 |
| $f = f_{2CSL}/1 - f_{3CSL}\%$ | 5.04 | 6.23 |

For reasons which will be discussed in the following section, we use here a rather high limiting value of $\Sigma 49$ for the distinction between CSL and random grain boundaries. We can conclude that both SG and LG samples have a very low fraction ($< 15\%$) of CSL grain boundaries and a high fraction of random grain boundaries. The fraction of the former in LG sample (13.31%) is slightly larger than that in SG sample (12.29%), but this difference is not significant.

In general, the fraction of CSLs in a microstructure is dependent on the stacking-fault energy of the material. Metallic polycrystals such as stainless steels have a low stacking-fault energy, resulting in a high fraction of CSLs [36]. Twinning often occurs when there are not enough slip systems to accommodate deformation or when the material has a very low stacking-fault energy. A fundamental effect of the twin formation on the CSL distributions is via the crystallographic constraints related to the CSL framework, i.e., the

so-called Σ -product rule, also named as coincidence index combination rule [27,36,37]. It describes that the integer product or quotient of the Σ values of any two CSLs connected at one triple junction is equal to the Σ value of the third CSL, i.e., $\Sigma_x \times \Sigma_y = \Sigma_{xy}$ or $\Sigma_x/\Sigma_y = \Sigma_{xy}$. This product rule is strictly valid only for triple junctions with three non-random grain boundaries and for the material with a cubic symmetry [27]. One typical example is the $\Sigma 3^n$ ($n = 1, 2, 3$) product effect, which indicates an interaction between $\Sigma 3$ -, $\Sigma 9$ - and $\Sigma 27$ -CSLs. If the fraction of $\Sigma 3$ -CSLs is increased through deformation and an annealing process, the corresponding fraction of $\Sigma 3^n$ type boundary increases and thus the microstructure is enhanced with increased resistant triple junction fraction [20,33].

In the further analysis of the grain boundary distribution in our LLZO pellets, the twin-characterized $\Sigma 3$ grain boundary is observed to have a small fraction, that is 1.42% in SG and 1.78% in LG, corresponding to the low fraction of the CSLs. The total fraction of $\Sigma 3^n$ -CSLs, which are dominant in a twin-limited microstructure [33], is 3.13% for SG and 3.34% for LG. As listed in Table 3, these fractions are much smaller than the total CSL fraction in each pellet and even far smaller than the $\Sigma 3^n$ -CSL fraction in the twinned metallic microstructure (> 20%) [20,33,38]. Furthermore, the fraction of the triple junctions with 3-CSLs in both pellets is $f_{3\text{CSL}} < 0.55\%$, which means that the possibility for a triple junction to have 3-CSLs connected is very small. Thus, we can conclude that the garnet type hot-pressed ceramic LLZO is not a twin-limited microstructure and the product rule for $\Sigma 3^n$ -CSLs is not applicable in the investigated samples. Aside from the absence of slip systems in LLZO, which describe the dominant energy scale for plasticity-driven recrystallisation in metallic systems, electrochemical aspects might also contribute to the found discrepancy between LLZO and metallic grain boundary resilience. Specifically, we note that recent investigations on grain boundary diffusivities have exhibited few cases of Li diffusivities lower in GBs than in the bulk for twin GBs and comparable to bulk diffusivity for certain types of screw GBs in LLZO, see Ref. [39,40]. The absence of a preference for low-energy states under long time tempering increases the number of fundamentally different characteristics between metallic and ceramic grain boundaries concerning transport properties [20,21,33,38].

Finally, Figure 7 presents the distributions of CSLs, random grain boundaries and different triple junction structures in the LLZO pellets.

The results are summarized in Table 3. We can see clearly the dominance of random grain boundaries and triple junctions with 0-CSL (>60%) and 1-CSL (>30%).

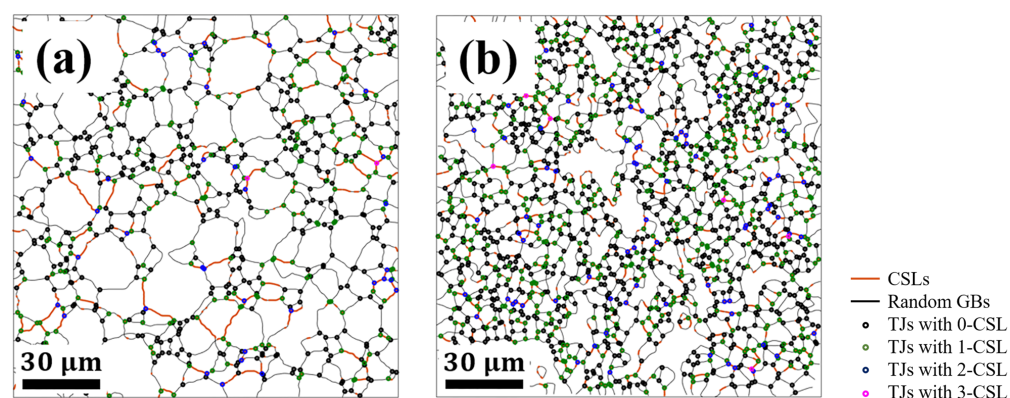


Figure 7. CSL grain boundaries ($\Sigma \leq 49$), random grain boundaries and different triple junction structures (with different numbers of connected CSLs) in the selected area of the pellets: (a) LG and (b) SG.

3.3. Percolation Hypothesis

In this section we return to the raised question, whether established grain boundary and triple junction percolation models, e.g., for corrosion or embrittlement in metallic

systems, could also be useful for failure in LLZO-based all-solid-state batteries. This question can now be addressed based on the extended analysis of the preceding section.

There is extended experimental evidence from the percolation analysis in the corrosion tests of stainless steel that the low- Σ CSLs, especially these with $\Sigma \leq 29$, have a higher resistance to percolating degradation than the random grain boundaries [20,21,33,38]. In contrast, the above results for LLZO show a clear dominance of random grain boundaries. To ensure a specific choice of a cutoff criterion between CSL grain boundaries that are considered as resistant, and random grain boundaries that may be susceptible to Li plating, is not affecting the result, we shift the transition between these two categories even up to $\Sigma 49$. The percolating paths in the microstructure are broken according to the conjecture if the resistant grain boundary fraction is larger than 65% (or susceptible grain boundary fraction is smaller than 35%) from the homogeneous bond percolation theory of the honeycomb lattice [20,30,31,33]. Obviously, with a random grain boundary fraction of about 87%, which is far above 35%, this criterion is fulfilled under all circumstances, hence percolation should always occur. We can therefore conclude that a distinction of grain boundaries according to CSLs and random grain boundaries does not lead to a applicable criterion to predict percolation-based failure of solid electrolytes. Aside from the honeycomb structure, we arrive at the same conclusion for a random network of either CSLs or random grain boundaries [20,41], with a slightly higher tendency for percolation in SG pellets. A consideration on the basis of resistant triple junction also leads to a similar picture. As suggested by Kumar [33], the fraction of resistant triple junctions is defined as $f = f_{2\text{CSL}}/1 - f_{3\text{CSL}}$ and is listed in Table 3. Here it is shown that the resistant triple junction fraction f and the CSL boundary fraction in SG samples are smaller than those in LG pellets, which is consistent with other publications [20,21]. From our results above, the fraction of resistant triple junctions of the pellets f (5.04% in SG, 6.23% in LG pellets) would be far smaller than the threshold for percolation suppression, contrary to the experimental findings that the majority of samples does not suffer from short-circuiting at the first battery cycles. However, LLZO-based all-solid-state batteries can still fail at post cycling stage due to intergranular Li penetration [4,42,43].

We can therefore conclude this section by the statement that a percolation criterion for Li plating based on the classification between resistant and susceptible grain boundaries similar to metallic systems does not seem to be appropriate. Nevertheless, the distinction of grain boundaries may still have an influence on the Li plating kinetics and could therefore affect the long term stability of solid electrolysis. This topic may be the subject of future investigations.

4. Conclusions

In this paper, the microstructure, and in particular the grain boundary and triple junction characteristics of LLZO hot-pressed pellets, which were synthesized using two different processing routes, were analyzed. Based on these results, an investigation of the transferability of a percolation-based failure model from metallic systems to ceramic solid electrolyte systems was performed. The key results are summarised as follows:

- The synthesis methods of the precursor powder and hot-pressed pellets are successful in producing large amounts of pure cubic phase of Ta:LLZO with very high relative density, the same composition and surface treatment, but with different grain size distributions, namely small grain (SG) and large grain (LG) samples.
- The fraction of CSL grain boundaries are slightly larger in the LG sample than those in the SG sample.
- The fraction of random grain boundaries is significantly higher than in typical metallic materials.
- Our investigations indicate that percolation-based failure criteria, which are successfully used, e.g., for corrosion of austenitic steels, cannot be applied for the prediction of Li plating along grain boundaries in LLZO as solid electrolytes. This conclusion

does however not exclude that different grain boundary characteristics can influence the delayed failure after long operation times.

Overall, the results suggest that the solid electrolyte LLZO is rather robust against Li penetration from the perspective of grain boundary percolation, and at least we do not find strong model-based arguments for such a failure mode. Therefore, the early manufacturing steps of the solid electrolyte, which are decisive for the grain structure, and which were proposed as origin for grain boundary percolation, are probably not competing with fracture induced failure during later fabrication and operation [6]. In turn, tuning of the grain structure may therefore be a suitable way to improve the mechanical stability of the solid electrolyte against fracturing or even to enable self-healing features.

Author Contributions: Conceptualization, S.F., C.H. and R.S.; methodology, S.F. and Y.A.; software, S.F.; validation, S.F., C.H. and R.S.; formal analysis, S.F.; investigation, S.F. and Y.A.; resources, M.F.; data curation, S.F.; writing—original draft preparation, S.F.; writing—review and editing, C.H. and R.S.; visualization, S.F.; supervision, R.S.; project administration, M.F. and R.S.; funding acquisition, M.F. and R.S. All authors have read and agreed to the published version of the manuscript.

Funding: This research was funded by the German Ministry of Research and Education (BMBF) in the framework of the project MEET Hi-End III. The authors gratefully acknowledge the computing time granted by the JARA Vergabegremium and provided on the JARA Partition part of the supercomputer JURECA at Forschungszentrum Jülich [44]. Open access was funded by the Deutsche Forschungsgemeinschaft (DFG, German Research Foundation)—491111487.

Data Availability Statement: The data presented in this study are available on request.

Acknowledgments: The authors would also like to especially thank to Alexander Schwedt, Fadli Rohman for the support of EBSD measurements and Stefan Neumeier for the support of hot-pressing.

Conflicts of Interest: There is no conflict to declare.

Abbreviations

The following abbreviations are used in this manuscript:

| | |
|---------|--|
| ASSB | All-Solid-State Batteries |
| LLZO | $\text{Li}_7\text{La}_3\text{Zr}_2\text{O}_{12}$ |
| EBSD | Electron Back Scatter Diffraction |
| CSL | Coincidence Site Lattice |
| LAGB | Low Angle Grain Boundary |
| GB | Grain Boundary |
| HP | Hot-Pressing |
| XRD | X-Ray Diffraction |
| ICP-OES | Inductively Coupled Plasma Optical Emission Spectroscopy |
| SEM | Scanning Emission Microscopy |
| MDF | Misorientation Density Function |
| TJ | Triple Junction |
| LG | Large Grain |
| SG | Small Grain |
| SSR | Solid-State Reaction |
| SASSR | Solution-Assisted Solid-State Reaction |

References

1. Goodenough, J.B. Rechargeable batteries: challenges old and new. *J. Solid State Electrochem.* **2012**, *16*, 2019–2029. [[CrossRef](#)]
2. Murugan, R.; Thangadurai, V.; Weppner, W. Fast lithium ion conduction in garnet-type $\text{Li}_7\text{La}_3\text{Zr}_2\text{O}_{12}$. *Angew. Chem. Int. Ed.* **2007**, *46*, 7778–7781. [[CrossRef](#)] [[PubMed](#)]
3. Arinicheva, Y.; Wolff, M.; Lobe, S.; Dellen, C.; Fattakhova-Rohlfing, D.; Guillon, O.; Böhm, D.; Zoller, F.; Schmuck, R.; Li, J.; et al. Ceramics for electrochemical storage. In *Advanced Ceramics for Energy Conversion and Storage*; Elsevier: Amsterdam, The Netherlands, 2020; pp. 549–709.

4. Motoyama, M.; Tanaka, Y.; Yamamoto, T.; Tsuchimine, N.; Kobayashi, S.; Iriyama, Y. The Active Interface of Ta-Doped Li₇La₃Zr₂O₁₂ for Li Plating/Stripping Revealed by Acid Aqueous Etching. *ACS Appl. Energy Mater.* **2019**, *2*, 6720–6731. [[CrossRef](#)]
5. Manthiram, A.; Yu, X.; Wang, S. Lithium battery chemistries enabled by solid-state electrolytes. *Nat. Rev. Mater.* **2017**, *2*, 1–16. [[CrossRef](#)]
6. McConohy, G.; Xu, X.; Cui, T.; Barks, E.; Wang, S.; Kaeli, E.; Melamed, C.; Gu, X.W.; Chueh, W.C. Mechanical regulation of lithium intrusion probability in garnet solid electrolytes. *Nat. Energy* **2023**, *8*, 241–250. [[CrossRef](#)]
7. Ren, Y.; Shen, Y.; Lin, Y.; Nan, C.W. Direct observation of lithium dendrites inside garnet-type lithium-ion solid electrolyte. *Electrochem. Commun.* **2015**, *57*, 27–30. [[CrossRef](#)]
8. Han, F.; Westover, A.S.; Yue, J.; Fan, X.; Wang, F.; Chi, M.; Leonard, D.N.; Dudney, N.J.; Wang, H.; Wang, C. High electronic conductivity as the origin of lithium dendrite formation within solid electrolytes. *Nat. Energy* **2019**, *4*, 187–196. [[CrossRef](#)]
9. Song, Y.; Yang, L.; Zhao, W.; Wang, Z.; Zhao, Y.; Wang, Z.; Zhao, Q.; Liu, H.; Pan, F. Revealing the short-circuiting mechanism of garnet-based solid-state electrolyte. *Adv. Energy Mater.* **2019**, *9*, 1900671. [[CrossRef](#)]
10. Cheng, E.J.; Sharafi, A.; Sakamoto, J. Intergranular Li metal propagation through polycrystalline Li_{6.25}Al_{0.25}La₃Zr₂O₁₂ ceramic electrolyte. *Electrochim. Acta* **2017**, *223*, 85–91. [[CrossRef](#)]
11. Sharafi, A.; Haslam, C.; Kerns, R.D.; Wolfenstine, J.; Sakamoto, J.S. Controlling and correlating the effect of grain size with the mechanical and electrochemical properties of Li₇La₃Zr₂O₁₂ solid-state electrolyte. *J. Mater. Chem.* **2017**, *5*, 21491–21504. [[CrossRef](#)]
12. Yonemoto, F.; Nishimura, A.; Motoyama, M.; Tsuchimine, N.; Kobayashi, S.; Iriyama, Y. Temperature effects on cycling stability of Li plating/stripping on Ta-doped Li₇La₃Zr₂O₁₂. *J. Power Sources* **2017**, *343*, 207–215. [[CrossRef](#)]
13. Tsai, C.L.; Roddatis, V.; Chandran, C.V.; Ma, Q.; Uhlenbruck, S.; Bram, M.; Heitjans, P.; Guillon, O. Li₇La₃Zr₂O₁₂ Interface Modification for Li Dendrite Prevention. *ACS Appl. Mater. Interfaces* **2016**, *8*, 10617–10626. [[CrossRef](#)] [[PubMed](#)]
14. Ren, Y.; Shen, Y.; Lin, Y.; Nan, C.W. Microstructure Manipulation for Enhancing the Resistance of Garnet-Type Solid Electrolytes to “Short Circuit” by Li Metal Anodes. *ACS Appl. Mater. Interfaces* **2019**, *11*, 5928–5937. [[CrossRef](#)]
15. Cheng, L.; Chen, W.; Kunz, M.; Persson, K.A.; Tamura, N.; Chen, G.; Doeff, M.M. Effect of surface microstructure on electrochemical performance of garnet solid electrolytes. *ACS Appl. Mater. Interfaces* **2015**, *7*, 2073–2081. [[CrossRef](#)]
16. Wells, D.B.; Stewart, J.; Herbert, A.W.; Scott, P.M.; Williams, D.E. The Use of Percolation Theory to Predict the Probability of Failure of Sensitized, Austenitic Stainless Steels by Intergranular Stress Corrosion Cracking. *Corrosion* **1989**, *45*, 649–660. [[CrossRef](#)]
17. Gaudett, M.A.; Scully, J.R. Applicability of bond percolation theory to intergranular stress-corrosion cracking of sensitized AISI 304 stainless steel. *Metall. Trans.* **1994**, *25*, 775–787. [[CrossRef](#)]
18. Perriot, R.; Uberuaga, B.P.; Zamora, R.J.; Perez, D.; Voter, A.F. Evidence for percolation diffusion of cations and reordering in disordered pyrochlore from accelerated molecular dynamics. *Nat. Commun.* **2017**, *8*, 618. [[CrossRef](#)] [[PubMed](#)]
19. Lee, J.; Urban, A.; Li, X.; Su, D.; Hautier, G.; Ceder, G. Unlocking the Potential of Cation-Disordered Oxides for Rechargeable Lithium Batteries. *Science* **2014**, *343*, 519–522. [[CrossRef](#)] [[PubMed](#)]
20. Tsurekawa, S.; Nakamichi, S.; Watanabe, T. Correlation of grain boundary connectivity with grain boundary character distribution in austenitic stainless steel. *Acta Mater.* **2006**, *54*, 3617–3626. [[CrossRef](#)]
21. Kobayashi, S.; Kobayashi, R.; Watanabe, T. Control of grain boundary connectivity based on fractal analysis for improvement of intergranular corrosion resistance in SUS316L austenitic stainless steel. *Acta Mater.* **2016**, *102*, 397–405. [[CrossRef](#)]
22. Tsai, C.L.; Dashjav, E.; Hammer, E.M.; Finsterbusch, M.; Tietz, F.; Uhlenbruck, S.; Buchkremer, H.P. High conductivity of mixed phase Al-substituted Li₇La₃Zr₂O₁₂. *J. Electroceramics* **2015**, *35*, 25–32. [[CrossRef](#)]
23. Mainprice, D.; Hielscher, R.; Schaeben, H. Calculating anisotropic physical properties from texture data using the MTEX open-source package. *Geol. Soc. Lond. Spec. Publ.* **2011**, *360*, 175–192. [[CrossRef](#)]
24. Kronberg, M.; Wilson, F. Secondary recrystallization in copper. *JOM* **1949**, *1*, 501–514. [[CrossRef](#)]
25. Brandon, D. The structure of high-angle grain boundaries. *Acta Metall.* **1966**, *14*, 1479–1484. [[CrossRef](#)]
26. Gottstein, G.; Shvindlerman, L. *Grain Boundary Migration in Metals: Thermodynamics, Kinetics, Applications*; Engineering & Technology, Physical Sciences, CRC Press: Boca Raton, FL, USA, 2009.
27. Priester, L. *Grain Boundaries: From Theory to Engineering*; Springer Series in Materials Science, Springer: Dordrecht, The Netherlands, 2013.
28. Fortier, P.; Aust, K.; Miller, W. Effects of symmetry, texture and topology on triple junction character distribution in polycrystalline materials. *Acta Metall. Mater.* **1995**, *43*, 339–349. [[CrossRef](#)]
29. Fortier, P.; Miller, W.; Aust, K. Triple junction and grain boundary character distributions in metallic materials. *Acta Mater.* **1997**, *45*, 3459–3467. [[CrossRef](#)]
30. Sykes, M.F.; Essam, J.W. Exact Critical Percolation Probabilities for Site and Bond Problems in Two Dimensions. *J. Math. Phys.* **1964**, *5*, 1117–1127. [[CrossRef](#)]
31. Stauffer, D.; Aharony, A. *Introduction to Percolation Theory*, 2nd ed.; Taylor & Francis: London, UK, 1992.
32. Frary, M.; Schuh*, C.A. Connectivity and percolation behaviour of grain boundary networks in three dimensions. *Philos. Mag.* **2005**, *85*, 1123–1143. [[CrossRef](#)]

33. Kumar, M.; King, W.E.; Schwartz, A.J. Modifications to the microstructural topology in fcc materials through thermomechanical processing. *Acta Mater.* **2000**, *48*, 2081–2091. [[CrossRef](#)]
34. Awaka, J.; Takashima, A.; Kataoka, K.; Kijima, N.; Idemoto, Y.; Akimoto, J. Crystal Structure of Fast Lithium-ion-conducting Cubic Li₇La₃Zr₂O₁₂. *Chem. Lett.* **2011**, *40*, 60–62. [[CrossRef](#)]
35. Mackenzie, J.K. Second paper on statistics associated with the random disorientation of cubes. *Biometrika* **1958**, *45*, 229–240. [[CrossRef](#)]
36. Don, J.; Majumdar, S. Creep cavitation and grain boundary structure in type 304 stainless steel. *Acta Metall.* **1986**, *34*, 961–967. [[CrossRef](#)]
37. Palumbo, G.; Aust, K.T.; Erb, U.; King, P.J.; Brennenstuhl, A.M.; Lichtenberger, P.C. On annealing twins and CSL distributions in F.C.C. polycrystals. *Phys. Status Solidi* **1992**, *131*, 425–428. [[CrossRef](#)]
38. Schuh, C.A.; Kumar, M.; King, W.E. Analysis of grain boundary networks and their evolution during grain boundary engineering. *Acta Mater.* **2003**, *51*, 687–700. [[CrossRef](#)]
39. Yu, S.; Siegel, D. Grain boundary contributions to Li-ion transport in the solid electrolyte Li₇La₃Zr₂O₁₂ (LLZO). *Chem. Mater.* **2017**, *29*, 9639–9647. [[CrossRef](#)]
40. Zhu, Y. Atomistic Modeling of Solid Interfaces in All-Solid-State Li-ion Batteries. Ph.D. Thesis, University of Maryland, College Park, MD, USA, 2018.
41. Ren, J.; Zhang, L.; Siegmund, S. How Inhomogeneous Site Percolation Works on Bethe Lattices: Theory and Application. *Sci. Rep.* **2016**, *6*, 22420. [[CrossRef](#)]
42. Aguesse, F.; Manalastas, W.; Buannic, L.; Lopez del Amo, J.M.; Singh, G.; Llordés, A.; Kilner, J. Investigating the dendritic growth during full cell cycling of garnet electrolyte in direct contact with Li metal. *ACS Appl. Mater. Interfaces* **2017**, *9*, 3808–3816. [[CrossRef](#)]
43. Liu, X.; Garcia-Mendez, R.; Lupini, A.R.; Cheng, Y.; Hood, Z.D.; Han, F.; Sharafi, A.; Idrobo, J.C.; Dudney, N.J.; Wang, C.; et al. Local electronic structure variation resulting in Li ‘filament’ formation within solid electrolytes. *Nat. Mater.* **2021**, *20*, 1485–1490. [[CrossRef](#)]
44. Krause, D.; Thörnig, P. JURECA: Modular supercomputer at Jülich Supercomputing Centre. *J. Large-Scale Res. Facil.* **2018**, *4*, 1–9. [[CrossRef](#)]

Disclaimer/Publisher’s Note: The statements, opinions and data contained in all publications are solely those of the individual author(s) and contributor(s) and not of MDPI and/or the editor(s). MDPI and/or the editor(s) disclaim responsibility for any injury to people or property resulting from any ideas, methods, instructions or products referred to in the content.